Solar Energy 311 (2026) 114537

Contents lists available at ScienceDirect

Solar Energy

journal homepage: www.elsevier.com/locate/solener

Mitigating the interference effects induced by optical cavities in superstrate thin-film silicon multi-junction solar cells

Govind Padmakumar*, Federica Saitta, K.P. Sreejith, Paula Perez-Rodriguez, René A.C.M.M. van Swaaij, Arno H.M. Smets

Photovoltaic Materials and Devices, Delft University of Technology Mekelweg 4, Delft, 2628CD, Zuid Holland, the Netherlands

HIGHLIGHTS

- Random and periodic textures are compared for interface scattering in a superstrate multijunction solar cell.
- Periodic arrays on glass perform better than random direct textured glass in light trapping for multijunctions.
- Grain scattering by thick sputtered zinc oxide can effectively mitigate the optical microcavities in multijunction solar cells.
- Wide bandgap TCOs like tin oxide can be used to facilitate grain scattering while reducing parasitic absorption of high-energy photons.

ARTICLE INFO

Keywords:
Optical cavity
Interference fringes
Solar cells
Sputtering
Honeycombs
Thin film silicon

ABSTRACT

A major challenge in multijunction devices is reduced light incoupling caused by interference fringes from optical microcavities. This paper reports a potential route to mitigate the interference effects with an effective front-window design. The concepts of interface scattering and grain scattering are implemented at the front side of superstrate tandem solar cells. A random texturing and periodic-hexagonal texturing approach on glass is used as interface scatterers. However, applying an interface scatterer alone is insufficient to eliminate the interference effects of optical cavities completely. Use of sputtered unintentionally doped zinc oxide (i-ZnO) or tin oxide (SnO) as grain scatterers stacked over random and periodic glass textures quenches the interference effects significantly. For a random textured glass substrate, a 1.5-μm thick i-ZnO layer could quench interference in the top cell, except for the effect of the optical cavity formed in the amorphous top cell. Hexagonal craters on glass, combined with a 0.9-μm thick i-ZnO layer, effectively mitigate fringes formed by all optical cavities in the device. This sample demonstrates the highest incoupled photon flux with 86% of photons entering the device. Use of a wide-bandgap grain scatterer, such as SnO, reduces parasitic absorption of high-energy photons while mitigating optical cavities. The design principles discussed in this work can be applied to any thin-film multijunction solar cells consisting of layers with contrasting refractive indices.

1. Introduction

In the energy transition, cost-effective yet efficient photovoltaic fabrication methods are required. Multijunction PV devices are considered a potential route to achieving these goals with low material utilisation and enhanced performance compared to conventional single-junction PV architectures [1,2]. Thin-film photoactive materials such as amorphous silicon (a-Si:H), copper indium gallium selenide (CIGS), organic PV, III-V materials or perovskites are combined with crystalline silicon wafers or another of the above-mentioned thin-film layers in a tandem configuration to form a multijunction solar cell. The choice of absorber combination depends on band gaps corresponding to the individual spectral utilisation potential and applications.

The complexity of the many layers of materials stacked to form a multijunction can introduce additional optical challenges [3]. The thin layers, stacked one on top of the other, can have alternating high- and low-refractive-index materials. This results in multiple reflecting surfaces within the device. These layers with contrasting refractive indices can form multiple Fabry-Pérot microcavities in the solar cell [4,5]. In an a-Si:H/nc-Si:H solar cell, the optical cavities (OC) can be identified as shown in Fig. 1. The constructive and destructive interferences of the

* Corresponding author.
Email address: g.padmakumar@tudelft.nl (G. Padmakumar).

https://doi.org/10.1016/j.solener.2026.114537
Received 10 December 2025; Received in revised form 6 February 2026; Accepted 17 March 2026
Available online 23 March 2026

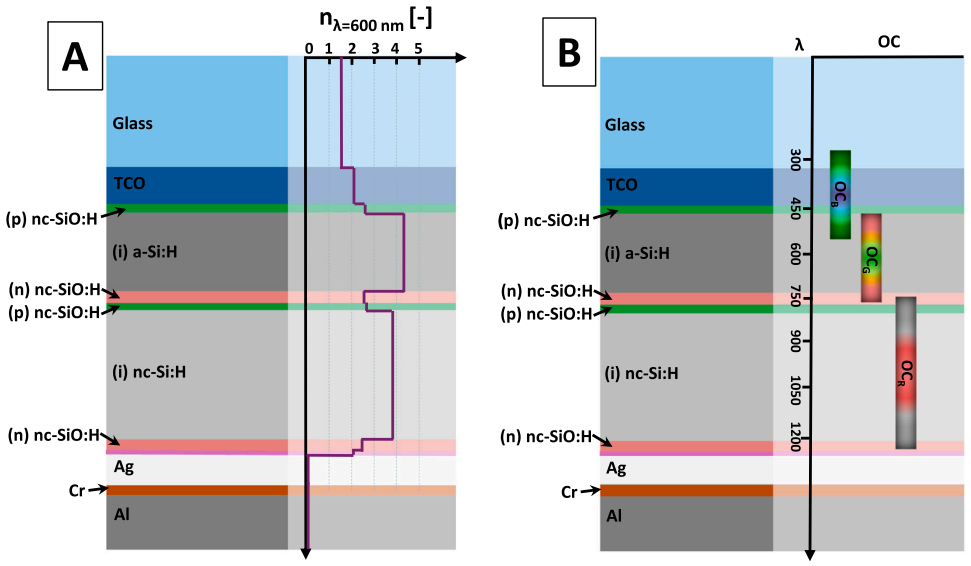

Fig. 1. Schematic representation of an a-Si:H/nc-Si:H double junction tandem solar cell. (A) The refractive index of each layer at a wavelength of 600 nm ($n_{\lambda=600}$) is overlaid on the image. A detailed wavelength versus refractive indices graph is given in Fig. 2. (B) The simplified demonstration of optical micro-cavities considering penetration depth of light with different wavelengths, is marked as OC_B, OC_G and OC_R.

(partially) coherent light might limit the light incoupling and absorption in the absorber layer at specific wavelengths. Which wavelengths (λ) interfere in which parts of the solar cell depends on how far light penetrates the stack of layers, determined by transmission and absorption at each λ. For example, an a-Si:H layer absorbs light up to λ corresponding to 1.8 eV and lets the remaining light pass through. This unabsorbed light is reflected between the layers. The multiple interference fringes in the spectral response reduce the absorption of photoactive layers in solar cells [6,7].

Three simplified OCs are identified and marked in the Fig. 1. OC_B is formed in the TCO and p-doped top layer, which has a low refractive index for wavelengths 300–550 nm (λs starting from blue) compared to that of a-Si:H top cell. OC_G is caused mainly by the high refractive index a-Si:H layer sandwiched between two low refractive index layers for wavelengths around 550–800 nm (λs starting from green), and OC_R is caused by the nc-Si:H silicon layer sandwiched between tunnelling recombination junction and nc-SiO:H/back reflector layer beyond 800 nm (λ corresponding to red and near infrared).

Standard techniques for mitigating interference in OCs are (i) light scattering via interface morphology ("interface-scattering") and (ii) light scattering aided with grains or crystals ("grain-scattering"). Interface-scattering is implemented in solar cells by texturing the front side [8] or the rear side of the solar cells [9,10], where the thin-film nature allows the other device interfaces to adopt the texture as well. Texturing increases the haze of the superstrates through effective scattering of light over broad wavelengths [11–13]. Grain scattering is implemented using transparent conductive oxides (TCO) layers with a thickness in the range of a few microns [14,15]. Polycrystalline materials like TCOs do not have uniform optical properties because of residual porosity, secondary phases, and/or crystalline anisotropies [16]. These optical inhomogeneities cause scattering in the bulk. The use of thicker TCO layers enhances light trapping, as the grains within the bulk effectively scatter incident light in transmission [17,18]. A combination of interface-scattering (from textured surfaces) and grain scattering (from thick TCO layers) at the front side has been employed in some of the highest-efficiency multijunction solar cells [19,20]. In this paper, we will study the extent to which a texture with or without grain scattering in the TCO bulk can mitigate coherent interference in the OCs in superstrate thin film silicon solar cells.

Chemical vapour deposition (CVD) techniques, such as low-pressure CVD (LPCVD), atmospheric pressure CVD (APCVD) and metal organic CVD (MOCVD) or physical vapour deposition (PVD) techniques like radio frequency (RF) and direct current (DC) sputtering, are commonly used to deposit TCO layers [18,19,21]. The processing methods and deposition temperature determine the presence of grains, crystallinity, grain shape and size. The TCO alloy's band gap and tail states determine its parasitic absorption of blue light and the transmission spectrum, respectively. State-of-the-art TCOs used in solar cells have been reported in literature by Hänni et al. where a 5-μm thick TCO layer is implemented on flat glass [15,17] and a 2.3-μm thick TCO layer by Tan et al. on micro-sized glass textures [19,22]. Both these approaches used i-ZnO deposited with LPCVD in superstrate configurations. On the module level, Cashmore et al. have reported a 2-μm boron-doped zinc oxide (BZO) grown using LPCVD as both front and rear electrodes [23–25]. These layers exhibit high-quality crystal growth but absorb UV light. PVD TCO deposition techniques, such as sputtering, result in TCO grain structure and properties very different from LPCVD depositions [17,26,27]. Often, they show more substantial absorbance for micron-thick TCO layers in the visible spectrum than LPCVD and MOCVD [18].

For the first time, this paper explores the use of grain scattering with sputtered TCOs and compares them with interface-scattering techniques to mitigate OCs. Interface scattering is investigated by implementing random and periodic surface texturings on glass substrates. Additionally, this paper addresses the extent to which TCO thickness can be reduced to implement grain scattering successfully. Increasing the layer thickness enhances the scattering of light by grains and reduces the electrical sheet resistance, but also increases the parasitic absorption in this layer. In this paper, we study a low-temperature (below 100 °C) deposited unintentionally doped zinc oxide (i-ZnO) and tin oxide (SnO), both deposited by RF magnetron sputtering and integrated at the front side of a-Si:H/nc-Si:H tandem solar cells. Grain scattering by TCO bulk was evaluated using varying thicknesses of sputtered i-ZnO layers. We propose a combined interface bulk design strategy on glass to suppress optical micro-cavity effects in a-Si:H/nc-Si:H tandem solar cells.

2. Experimental details

2.1. Deposition of layers in a-Si:H/nc-Si:H tandem solar cells

The a-Si:H/nc-Si:H tandem devices were co-deposited in a superstrate p-i-n top cell /p-i-n bottom cell architecture similar to Fig. 1. All solar cells are measured without any external anti-reflection coating (ARC).

Absorber layers: The deposition of intrinsic hydrogenated nanocrystalline silicon ((i)nc-Si:H) and amorphous silicon ((i)a-Si:H) absorbers was made in a PECVD multichamber tool at very high frequency (40.68 MHz) and 170 °C substrate temperature. A thin seed layer (SC = 1%) is used for facilitating nucleation sites [28] during the nc-Si:H bottom cell depositions.

Doped layers: Using B_2H_6 and pH_3 as dopant gases, boron-doped p-layer and phosphorus-doped n-layer were deposited at RF (13.8 MHz) and 180 °C substrate temperature in dedicated chambers. The p-doped layers at the front consist of a thin, heavily boron-doped silicon oxide contact layer ((p+)nc-SiO:H) and a boron-doped silicon oxide window layer ((p)nc-SiO:H). A similar configuration of p-layers is also used in the tunnelling recombination junction (TRJ) with a higher oxygen content in its layers. The n-doped TRJ consists of three layers: phosphorus-doped amorphous silicon ((n)a-Si:H), phosphorus-doped heavily oxygenated silicon oxide layer ((n)nc-SiO:H) and a phosphorus-doped nc-Si:H contact layer ((n)nc-Si:H). The nc-SiO:H layer in TRJ is 70 nm thick, acting as an intermediate reflectance layer as well [29,30]. A similar order of n-doped layers is used for the rear side of the bottom cell. The nc-SiO:H layer at the rear side is 30 nm thick.

Back reflector, contacts: The back reflector (BR) consists of sputtered i-ZnO (60 nm) and an evaporated silver (300 nm) layer. An aluminium strip serves as the front contact for these solar cells, and the back contact consists of 5 mm × 5 mm square-shaped chromium (30 nm) and aluminium (500 nm) dots.

The above mentioned layers result in a solar cell structure: TCO front electrode/(p+)nc-SiO:H /(p)nc-SiO:H /(i)a-Si:H /(n)a-Si:H /(n)nc-SiO:H /(n)nc-Si:H /(p+)nc-SiO:H/(p)nc-SiO:H /(i)nc-Si:H/(n)a-Si:H/(n)nc-SiO:H/(n) nc-Si:H /BR. The deposition conditions of all layers for the a-Si:H/nc-Si:H tandem solar cells with their thicknesses are given in Table 1. The rows from top to bottom follow the order of deposition.

2.2. Design of experiment

2.2.1. Textured glass substrates

The superstrate tandem solar cells are made on two different glass textures: (i) random texture, named superimposed texture (SIT), and (ii) periodic hexagonal-shaped textures, also known as honeycomb (HC) textures. Both textures are created directly on Corning borosilicate glass XG.

SIT is a type of multiscale texture developed directly on glass by generating nano-sized features on micro-sized textures through a sequential wet-etching process. The procedure of developing SIT is given in 7 steps as discussed. In Step 1, Corning XG glass is cleaned in ultrasonic baths of acetone and 2-propanol for 10 minutes each. During Step 2, ITO is deposited as a sacrificial TCO layer using magnetron sputtering at an elevated temperature. In subsequent Step 3, the layer deposited on the flat glass is wet-etched with hydrofluoric acid (HF) (40%): H_2O_2(31%): H_2O in the ratio 1:2:10. In this step ITO layer acts as a selective leaking mask and solution etches glass to make micrometer scale textures on the glass surface. The etching is continued until the ITO layer is completely removed. In next Step 5, an i-ZnO layer is deposited as a sacrificial TCO layer over the textured surface using magnetron sputtering (at an elevated temperature). In Step 6, the i-ZnO layer is wet-etched using an HF (40%) and nitric acid (HNO_3) (69.9%) solution in a 1:8 ratio. In Step 7, the substrate is cleaned to remove any residual TCO by dipping it in HNO_3 (69.9%) for 3 minutes. The detailed procedure and properties are reported elsewhere [12]. The RMS roughness of SIT is approximately 400 nm. For this SIT, a total spectral utilisation potential of 26.7 mA/cm^2 is demonstrated on an nc-Si:H single-junction solar cell without ARC (after quenching effect of all OCs in the device) [12].

HC textures are created on glass using photolithography (with specific masks) and wet etching in 9 subsequent steps. UV photolithography is used to generate HC textures on the glass substrates. In Step 1, the Corning glass wafer is cleaned with 69.5% HNO_3 for 3 minutes. In Step 2, the wafer is dried at 110 °C. In Step 3, the wafer is exposed to hexamethyl disilazane (HMDS) for 150 s at 150 °C, using nitrogen as the carrier gas. In Step 4, Shipley SPR3012 positive photoresist (2.1 μm thick) is spin-coated. In Step 5, UV exposure is conducted using a chromium reticle with periodically distributed holes. Step 6 involves pattern development, in which the exposed areas of the photoresist are removed. The photolithography technique implemented on glass requires an additional hard-bake at 140 °C for 30 min as Step 7. In Step 8, the pattern is transferred from the mask to the Corning glass wafer through a 20-minute dip in premade buffered hydrofluoric acid, comprised of ammonium fluoride (NH_4F) (40%): hydrofluoric acid (HF) (49%) in ratio of 7:1. The wafer is then rinsed with deionised water, and the remaining photoresist is removed. The detailed procedure and process optimisation are described elsewhere [31]. The HC substrates used in this paper have a periodicity of 5-μm and a texture depth of 1-μm. For this HC, a 3200-nm thick nc-Si:H single-junction solar cell

Table 1
Deposition conditions of different silicon-based layers in the solar cell. The distance between the RF electrode and the grounded electrode is 13 mm for all p-doped layer depositions, 13 mm for all intrinsic layer depositions, and 21 mm for all n-doped layer depositions.

Layer	SiH_4 [sccm]	H_2 [sccm]	Dopant Gas [sccm]	CO_2 [sccm]	Pressure [mBar]	Power [W/cm^2]	Thickness [nm]	epo. rate [Å/s]
(p+)nc-SiO:H (contact)	0.8	170	50 (0.02% B_2H_6 in H_2)	1.2	2.2	0.12	3	0.46
(p)nc-SiO:H (window)	0.8	170	10 (0.02% B_2H_6 in H_2)	1.2	2.2	0.12	13	0.39
(i)a-Si:H	6	120	–	–	5	0.30	280	4.0
(n)a-Si:H (TRJ)	40	0	11 (2% pH_3 in H_2)	0	0.6	0.04	5	1.1
(n)nc-SiO:H (TRJ/RL)	1	120	2 (2% pH_3 in H_2)	2.4	1.5	0.11	70	0.11
(n)nc-Si:H (TRJ)	1	120	2 (2% pH_3 in H_2)	0	1.5	0.11	7	0.19
(p+)nc-SiO:H (TRJ)	0.8	170	50 (0.02% B_2H_6 in H_2)	2.2	2.2	0.12	3	0.46
(p)nc-SiO:H (TRJ)	0.8	170	10 (0.02% B_2H_6 in H_2)	2.2	2.2	0.12	15	0.39
(i)nc-Si:H (seed)	1.1	120	–	–	4	0.4	90	2.25
(i)nc-Si:H (bulk)	3.2	120	–	–	4	0.4	3200	4.82
(n)a-Si:H	40	0	11 (2% pH_3 in H_2)	0	0.6	0.04	5	1.1
(n)nc-SiO:H	1	120	2 (2% pH_3 in H_2)	1.6	1.5	0.11	30	0.22
(n)nc-Si:H (contact)	1	120	2 (2% pH_3 in H_2)	1.6	1.5	0.11	7	0.19

fabricated has demonstrated a potential to obtain 28.6 mA/cm^2 current (after quenching the effect of all OCs) [32,33].

2.2.2. Front electrode design

The TCO front electrode design is based on the bandgap of the TCOs and the phenomenon that we want to observe.

(i) To observe interface scattering: A single layer 150-nm thick hydrogenated indium oxide (IOH) electrode. IOH layer is amorphous, with no grain structures to contribute to any light scattering inside its bulk. Amorphous IOH is a "flat" layer and adopts the texture of the substrate on which it is deposited [18]. For this reason, IOH is chosen to study interface scattering.

(ii) To study grain scatterer which is a part of the front electrode: Sputtered i-ZnO has a low band gap, which permits its use as a grain scatterer in a "bi-layer" (BL) configuration. BL front electrode stack comprises a thick i-ZnO layer deposited on top of amorphous IOH over glass. Both IOH and i-ZnO are deposited with RF magnetron sputtering. i-ZnO has a crystalline structure with columnar grains. It can facilitate light scattering at the bulk grains. It is added to the IOH layer that has a low sheet resistance. In this BL configuration, charge transport is expected to occur laterally in IOH layers and transversely through i-ZnO columns [18]. Varying the layer thickness of i-ZnO is expected to enhance grain scattering.

(iii) To study grain scatterer, which is a part of the substrate: HC texture is also studied with a SnO layer to act as a grain scatterer. SnO is a wide bandgap TCO with very high sheet resistance. The presence of SnO in a silicon cell creates an energy barrier in the valence band for holes at the SnO/p-doped layer interface due to the very high bandgap relative to the (p)nc-SiO:H. The wide bandgap of SnO prevents its use in a bi-layer TCO configuration, unlike i-ZnO. To overcome this effect, the SnO layer is deposited directly on glass, making it a part of the substrate. The thick SnO layer is electrically isolated from the solar cell stack using a 100 nm thick silicon oxide layer deposited at 400 °C.

Deposition conditions and the bandgap of the TCO layers are specified in Table 2. Additionally, the refractive indices and extinction coefficients of all materials used in this study are given in Fig. 2(A) and (B) as a function of λ.

The a-Si:H/nc-Si:H tandem solar cells made on SIT with only IOH as TCO layer are referred to as SIT-IOH. Tandem cells made on SIT, with IOH (150 nm)/i-ZnO (1500 nm) bi-layer TCO will be referred to as SIT-BL. The device structures are illustrated in Fig. 3(A), (B). Similarly, a-Si:H/nc-Si:H tandem solar cells made on HC with IOH TCO are referred to as HC-IOH, and tandem cells made on HC with IOH (150 nm)/i-ZnO bi-layer TCO are referred to as HC-BL. In this case, the amorphous top layer is expected to smooth the nano-features in the textures, and the bottom layer's spectral utilisation is maximised with micro-sized textures [19]. The device structures are illustrated in Fig. 3(C), (D). The tandem solar cell made on HC with electrically isolated SnO used as a grain scatterer is referred to as HC-SnO. The structure of this device is illustrated in Fig. 3(E). Four experiments are performed in total, using nine solar cells with structures as summarised in Table 3.

2.3. Texture and Solar cell characterisation

The textures on glass are analysed using atomic force microscopy (AFM) with a Bruker AFM FastScan in FastScan closed-loop scanner head mode. Power spectral density of 16-μm × 16-μm is extracted using NanoScope Analysis (version 2.0) software from Bruker. In addition, scanning electron microscopy (SEM) with Hitachi Regulus 8230 at an acceleration voltage of 1.5 kV (to minimise charging of glass) is used to create cross-sectional images of solar cells on glass. The open-circuit voltage (V_{oc}) and fill factor (FF) of solar cells were measured by a WACOM-class AAA xenon-halogen dual lamp continuous AM1.5G spectral simulator at 25 °C. The short-circuit current density (J_{sc}) values were calculated based on the EQE measurement by integrating over the AM1.5G solar spectrum. In this way, the effect of any mismatch between the solar simulator spectrum and the AM1.5 spectrum is prevented. Also, it eliminates any overestimation of current caused by errors in estimating the active cell area in small-area solar cells. EQE measurements were performed using an in–house developed system equipped with monochromatic illumination and an EQE calibration photodiode from Fraunhofer ISE. For multijunction solar cells, each subcell was characterised under carefully selected high-intensity bias light (LED sources) and at 0 V. The total reflection spectra (R) of the solar cell are recorded using a LAMBDA 1050+ UV/Vis/NIR Spectrophotometer with a 150-mm InGaAs integrating sphere from PerkinElmer for a 300 to 1200 nm λ range at 10-nm intervals.

In this paper, a parameter $R'_{\lambda_1<\lambda<\lambda_2}$, signifying the fraction of total photons reflected in the wavelength range between $\lambda 1$ and $\lambda 2$ in the AM1.5 solar spectrum, is calculated following the equation:

$$R'_{\lambda_1<\lambda<\lambda_2}(\%) = \frac{\int_{\lambda_1}^{\lambda_2} R(\lambda)\Phi(\lambda)\,d\lambda}{\int_{300}^{1200} \Phi(\lambda)\,d\lambda} \times 100\% \quad (1)$$

Where $R(\lambda)$ is the measured reflectance of the solar cell and $\Phi(\lambda)$ is the photon flux density of the AM1.5 spectrum, as a function of λ. For evaluating optical cavities - OC_B, OC_G and OC_R, weighted average reflectance $R'_{300<\lambda<540}$, $R'_{550<\lambda<790}$ and $R'_{800<\lambda<1200}$ were used respectively.

3. Results and discussion

3.1. Inspection of interfaces and i-ZnO grains

Fig. 4 shows the cross-section SEM images of SIT-IOH, SIT-BL, HC-IOH and HC-BL4, respectively. The growth of i-ZnO crystals on both substrates is similar. Additionally, the growth of i-ZnO crystals from small to large crystals with increasing thickness is evident in the SEM of SIT-BL. At the specific thickness of 0.9-μm (marked in the image), the cross-sectional grain structure and size of i-ZnO on both types of textures (SIT-BL and HC-BL4) appear identical.

Table 2
Deposition conditions of TCO front electrode and back reflector TCO layer. T_{sub} refers to substrate temperature. Band gap is determined from Tauc plot analysis of the TCO.

TCO	Ar [sccm]	H_2O Partial Pressure	Pressure [μBar]	Power [W/cm^2]	T_{sub} (°C)	Thickness [nm]	Depo. Rate [Å/s]	Bandgap [eV]
IOH (Front electrode)	50	0.06	5.7	1.5	27	150	0.98	3.9
i-ZnO (Front electrode)	20	–	2.6	2.0	95	varied	0.87	3.1
i-ZnO (Back Reflector)	20	–	2.6	2.0	157	60	0.87	3.2
	Ar [sccm]	Ar/O_2 [sccm]						
SnO (Grain Scatterer)	10	10	2.6	1.5	95	60	0.7	3.9

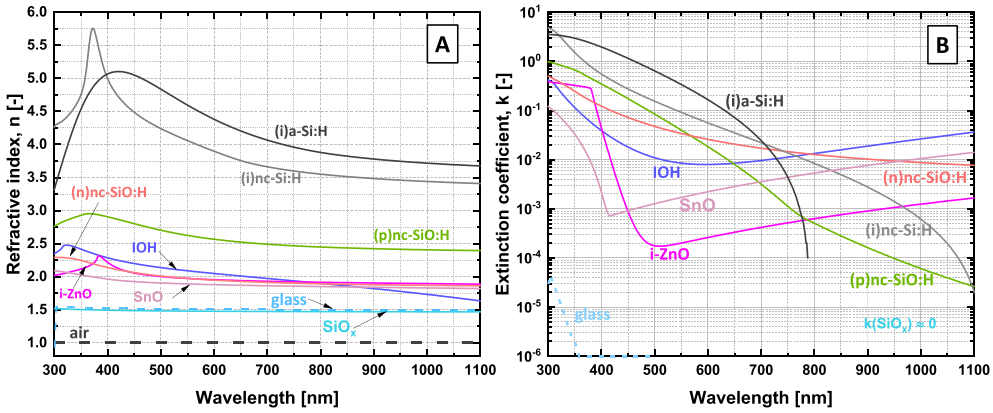

Fig. 2. The (A) refractive index - n, and (B) extinction coefficient - k, of materials in this study.

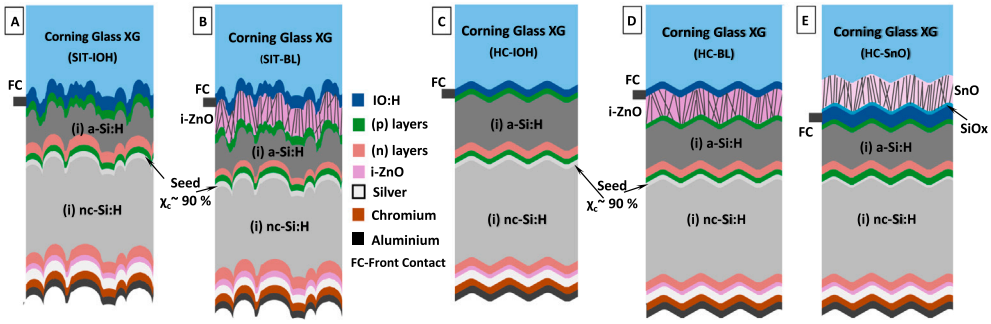

Fig. 3. A-Si:H/nc-Si:H superstrate tandem solar cells on (A) random textured glass: SIT-IOH (B) random textured glass with thick front i-ZnO: SIT-BL (C) periodic textured glass: HC-IOH (D) periodic textured glass with thick front i-ZnO: HC-BL (E) periodic textured glass with SnO/SiOx at front: HC-SnO.

Table 3
List of samples, figures, substrates, and corresponding experimental objectives for tandem solar cell studies.

Serial Number	Sample	Figure	Substrate	i-ZnO thickness [μm]	Experiment
1	SIT-IOH	1(A)	Random	0	To study the difference in random textures interface and interface-grain combination scattering.
2	SIT-BL	1(B)	Random	1.5	
3	HC-IOH	1(C)	Periodic	0	To study the influence of grain scattering combined with periodic textures.
4	HC-BL1	1(D)	Periodic	0.2	
5	HC-BL2	1(D)	Periodic	0.4	
6	HC-BL3	1(D)	Periodic	0.6	
7	HC-IOH	1(C)	Periodic	0	To study the difference in periodic textures interface and interface-grain combination scattering.
8	HC-BL4	1(D)	Periodic	0.9	
				SnO thickness [μm]	Experiment
9	HC-SnO	1(E)	Periodic	1.0	To study the influence of wide band gap grain scatterers.

Fig. 5(A) gives the power spectral density (PSD) of SIT-IOH and HC-IOH. Zone 1 represents the large-sized features in the texture morphology, while Zone 2 represents the small features. In both zones, HC-IOH has a higher value than SIT-IOH, suggesting that HC-IOH has more features at micro- and nano-scale [11]. These features actively scatter light over a broad wavelength range. Fig. 5(B) is the surface angle distribution of SIT-IOH and HC-IOH superstrates. HC-IOH shows a concentrated peak at 17°, whereas SIT-IOH shows a broad distribution with a peak at 12°. This sharp peak indicates that HC-IOH has a uniform taper, leading to gradual changes in optical density and improved light coupling [34,35].

3.2. a-Si:H / nc-Si:H tandem solar cells on random textures

Fig. 6(A) shows the EQE of tandem solar cells made on SIT. The interface-scattering in SIT is insufficient to mitigate the fringes in the solar-cell stack. Thus, SIT-IOH has the effect of OC_B, OC_G and OC_R in the $1 - R$ spectra, resulting in multiple fringes across the entire wavelength range. The effect of interference fringes is directly translated to the EQE spectra, leading to a loss of optical response. The top cell loses the response in OC_B at around $400 - 500$ nm, and OC_G reduces the bottom cell response at a wavelength of approximately 750 nm (marked with arrows). A total spectral utilisation ($J_{SC,TOT}$) of a-Si:H / nc-Si:H tandem on SIT-IOH is 24.7 mA/cm^2.

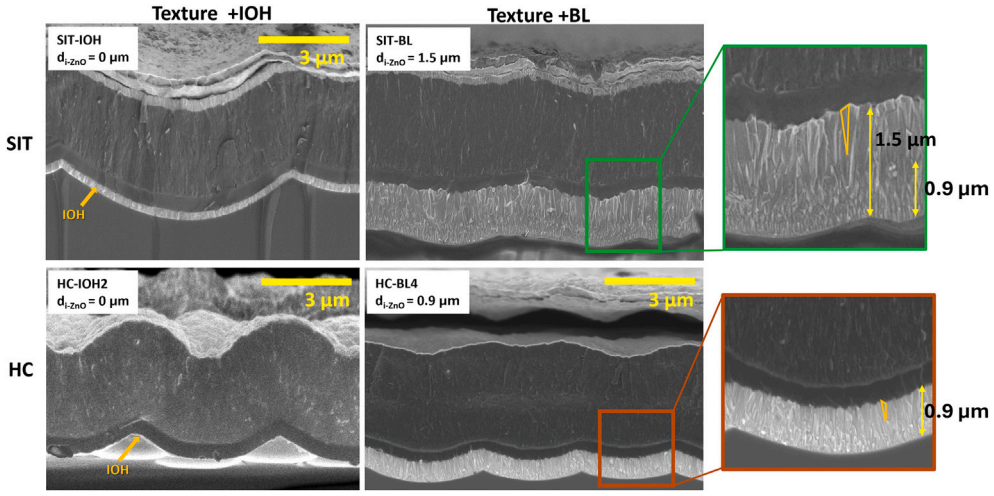

Fig. 4. Cross-sectional SEM images of a-Si:H/nc-Si:H tandem solar cells made on SIT-IOH, SIT-BL (1.5-µm thick i-ZnO), HC-IOH and HC-BL4 (0.9-µm thick i-ZnO). The i-ZnO layer is zoomed in with its heights marked, and one crystal is also marked (arbitrarily selected) to guide the reader. Note: The profile in HC solar cells in HC-BL4 differs from that in HC-IOH because the cut in the glass is not exactly through the lowest point of the hexagons.

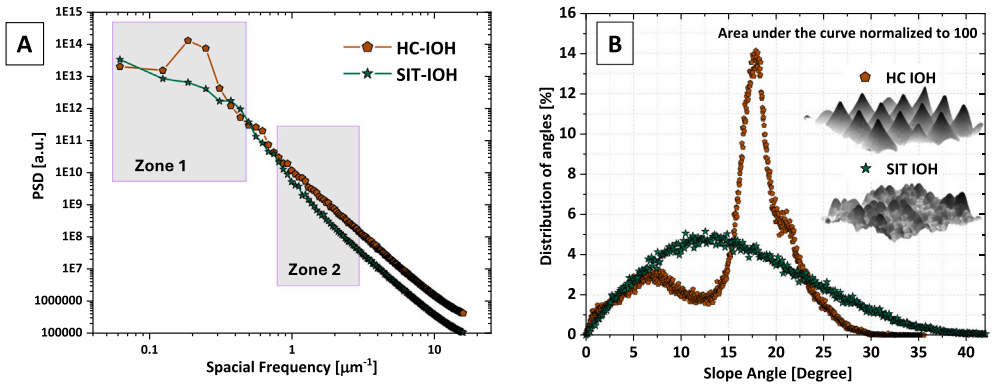

Fig. 5. (A) PSD of SIT and HC textures. (B) Slope distribution of SIT and HC textures, the 3D isometric view of the textures is given inset.

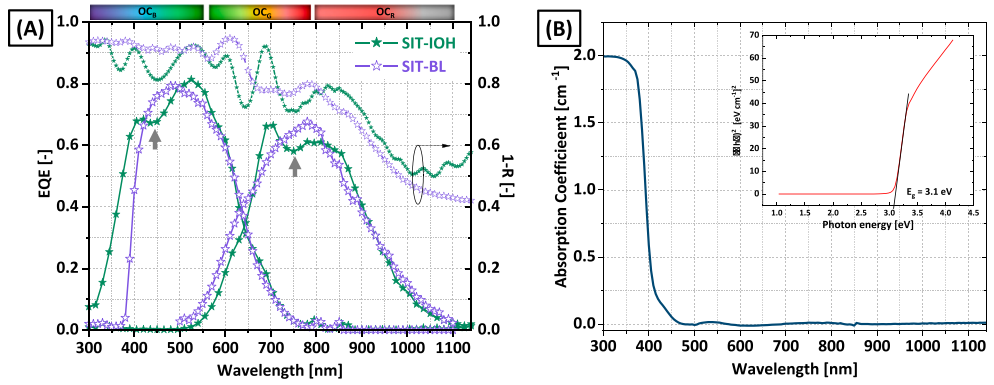

Fig. 6. (A) EQE and $1 - R$ spectra of SIT-IOH and SIT-BL a-Si:H/nc-Si:H tandem solar cells (B) Absorptance of i-ZnO used in SIT-BL.

To study the optical effects of SIT combined with grain-scattering in multijunction solar cells, a 1.5-µm thick i-ZnO layer is added to the front electrode, forming a bi-layer. Fig. 6(B) shows the estimated bandgap and absorption coefficient (α) of i-ZnO. The estimated bandgap of sputtered i-ZnO is 3.1 eV, which corresponds to λ =399 nm. Photons with energies above this threshold are absorbed in i-ZnO. Similarly, minor parasitic absorption loss is observed between λ =400 nm and 500 nm due to tail states in sputtered i-ZnO [18].

EQE spectra of SIT-BL in Fig. 6(A) suggest that at the shorter wavelengths, the amplitude of interference fringes in the $1 - R$ spectra due to OC_B were reduced with the bi-Layer TCO. The fringes resulting from the IOH/(p)SiO:H layer are reduced, showing that the light has become less coherent (also, a minor reduction in reflection at the TCO/silicon interface is also achieved by the introduction of i-ZnO due to graded refractive index values; however, this effect is not a significant factor here). This leads to the conclusion that grain-scattering is needed to

Table 4
Weighted average reflectance values R' of different solar cells presented in this paper.

Sample	$R'_{300<\lambda<540}$ [%]	$R'_{550<\lambda<790}$ [%]	$R'_{800<\lambda<1200}$ [%]	$R'_{300<\lambda<1200}$ [%]
SIT-IOH	3.24	8.88	8.63	20.75
SIT-BL	2.24	7.47	10.03	19.74
HC-IOH	2.37	6.47	9.87	18.71
HC-BL1	2.19	6.06	10.49	18.74
HC-BL2	2.16	6.01	9.47	17.64
HC-BL3	2.10	5.40	10.11	17.61
HC-BL4	1.93	4.10	8.02	14.05
HC-SnO	1.58	5.29	10.15	17.01

mitigate interference fringes in OC_B in SIT. Yet, the SIT interface and grain-scattering combination is unable to break the OC_G formed by the flat a-Si:H top cell. Table 4 gives the R' values for SIT-IOH and SIT-BL. Both $R'_{300<\lambda<550}$ and $R'_{550<\lambda<790}$ are decreased when i-ZnO is incorporated into IOH as a TCO layer, indicating a better light incoupling as a result of reduced interferences in the layers.

The benefit of light trapping in the solar cell with bi-layer TCO is nullified by the parasitic absorption losses of high-energy photons in i-ZnO. As a consequence, $J_{SC,TOT}$ of SIT-BL is 24.5 mA/cm^2 which is 0.2 mA/cm^2 less than that of SIT-IOH. The sputtered i-ZnO with a thickness of 1.5-μm is insufficient to completely mitigate the Fabry-Pérot interference effects in solar cells with random textures, unlike the LPCV-deposited i-ZnO reported in the literature [8]. This is due to the fact that CVD-grown TCOs have more crystal grains in the bulk. Moreover, these CVD-grown TCOs are optically more transparent and have higher electrical conductivity than RF magnetron-sputtered TCOs, as sputtering is heavily dependent on target quality [26,27].

3.3. a-Si:H / nc-Si:H tandem solar cells on periodic textures

For studying a bi-layer TCO structure on HCs, i-ZnO layers with thicknesses of 0.2 μm, 0.4 μm, and 0.6 μm were incorporated, named HC-BL1, HC-BL2, and HC-BL3, respectively.

Fig. 7(A) shows SEM images of the superstrate glasses before deposition. It can be observed that the size of TCO crystals increases with increasing layer thickness. This observation is consistent with what is reported by Faÿ et al. [17]. Solar cell active layer stack of HC-BL1, HC-BL2, and HC-BL3 was fabricated together with HC-IOH in a single batch to ensure comparability.

Fig. 7(B) gives the $1-R$ of the solar cells. Considering the $1-R$ spectra, it is observed that, with increasing thickness and crystal size, the bi-layer TCO reduces the fringe amplitudes. Table 4 gives the R' values corresponding to different optical cavities for HC-IOH, HC-BL1, HC-BL2, and HC-BL3. HC-BL1 shows a minor shift of fringe from 350 to 420 nm because i-ZnO absorbs all photons below 380 nm completely. The interference fringe pattern in the 1-R is approximately the same for HC-IOH and HC-BL1. For HC-BL2 and HC-BL3, the fringes formed by OC_B are totally quenched. This indicates that at least an i-ZnO thickness of 0.4-μm (as in HC-BL2) is required to diminish the effect of OC_B in hexagonal micro-textures. $R'_{300<\lambda<540}$ consistently decreases in value, indicating the decrease in reflected photon flux in the blue region. It is also observed that even a 0.6-μm thick i-ZnO is not enough to mitigate the interference in OC_G. However, $R'_{550<\lambda<790}$ decreases by $\approx$ 1% absolute when 0.6-μm i-ZnO layer is introduced. No tandem solar cells on the HC textures show major interference in the near-infrared. This is either because the interface scattering of 5-μm periodic HC with 1-μm height profile can mitigate OC_R, or because the bottom cell thickness is sufficient to absorb all low-energy photons.

Fig. 7(B) also gives the sub-cell EQEs. HC-IOH, HC-BL1, HC-BL2 and HC-BL3 have total spectral utilisations of 26.7 mA/cm^2, 25.8 mA/cm^2, 25.3 mA/cm^2 and 24.7 mA/cm^2 respectively. Table 5 gives the photoresponse at different λ ranges. The $J_{SC,TOT}$ continuously decreases with an increase in i-ZnO thickness due to loss in blue response (related to bandgap) and parasitic absorption in the visible range by i-ZnO (related to tail states in i-ZnO). A loss of 0.6 mA/cm^2 is observed directly in $J_{\lambda<450nm}$ as parasitic absorption with the addition of 200-nm thick i-ZnO. The loss in the IR region is due to free carrier absorption (Drude absorption) [36].

Fig. 8 gives the EQE and $1-R$ of tandem solar cells made on HC-IOH and HC-BL4. Initially, we consider the sole effect of the periodic and random interface scatterings by comparing HC-IOH with SIT-IOH (from Fig. 6). In HC-IOH, the amplitude of fringes is significantly diminished compared to HC-IOH. This is due to the morphological properties of HC-IOH shown in Fig. 5 and discussed in Section 3.1. The presence of more feature sizes enhances scattering in HC-IOH compared to SIT-IOH.

Table 5
$J_{sc,TOT}$ and constituting component current values of solar cells on HC-IOH, HC-BL1, HC-BL2, and HC-BL3 samples. NB: Subscripts - ToC refers to the top cell, and BoC refers to the bottom cell.

Sample	d_{i-ZnO} [μm]	$J_{\lambda<450nm}$ [mA/cm^2]	$J_{sc,ToC}$ [mA/cm^2]	$J_{sc,BoC}$ [mA/cm^2]	$J_{\lambda>900nm}$ [mA/cm^2]	$J_{sc,TOT}$ [mA/cm^2]
HC-IOH	0	2.7	10.0	16.8	1.9	26.8
HC-BL1	0.2	2.1	9.1	16.7	1.7	25.8
HC-BL2	0.4	1.8	9.6	15.7	1.5	25.3
HC-BL3	0.6	1.9	9.6	15.1	1.5	24.7

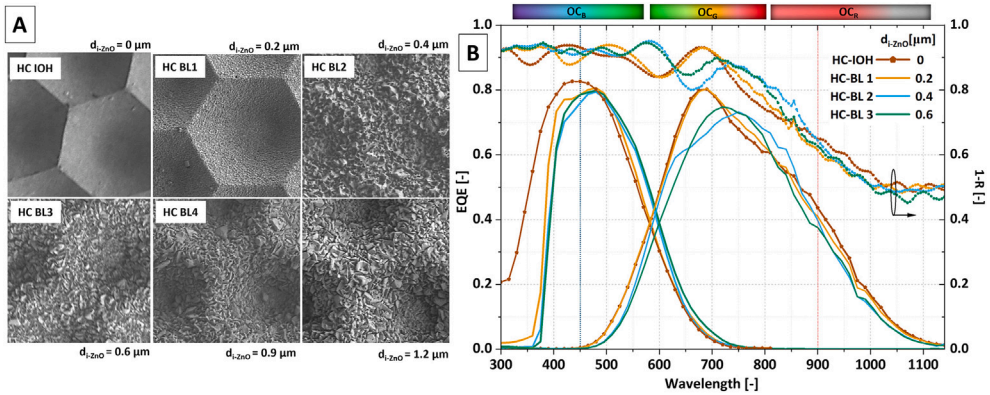

Fig. 7. (A) SEM images of different substrates used for HC-IOH (covered glass), HC-BL1 (200 nm thick i-ZnO), HC-BL2 (400 nm thick i-ZnO), HC-BL3 (600 nm thick i-ZnO) and HC-BL4 (0.9-μm thick i-ZnO). Additionally, 1.5-μm thick i-ZnO layer on glass is shown to demonstrate the size difference in crystals. (B) EQE and $1-R$ spectra of a-Si:H/nc-Si:H tandem solar cells on these superstrates.

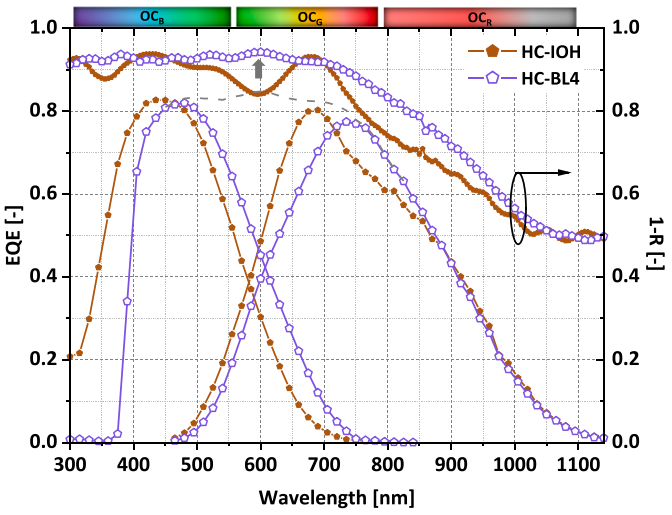

Fig. 8. EQE and $1 - R$ spectra of HC-IOH and HC-BL4 a-Si:H/nc-Si:H tandem solar cells. Dotted lines represent the total spectral utilisation of HC-BL4.

Additionally, light coupling via tapered gratings reduces reflection in the cavities. Table 4 shows a gain of approximately 1% and more than 2% in $R'_{300<\lambda<540}$ and $R'_{550<\lambda<790}$ respectively for HC-IOH over SIT-IOH and an overall R' increase of 2% incoupled photon flux.

As discussed before, 0.4-μm i-ZnO bi-layer mitigates the OC_B in HC substrates. A further increase in i-ZnO thickness up to 0.9-μm could mitigate the OC_G as well (marked with an arrow). HC-BL4 suggests that the OCs in HC superstrates can be nullified by scattering from smaller grains compared to SITs (refer to SEM image Fig. 4). This can be attributed to the efficient interface-scattering property of HC, which, in turn, requires a smaller grain size to mitigate all OCs. From Table 4, an increase of 0.4%, 2.3% and 1.8% gain in photon flux is observed for $R'_{300<\lambda<540}$, $R'_{550<\lambda<800}$, and $R'_{800<\lambda<1200}$ respectively resulting in an overall gain of 4.6% in photon flux in HC-BL4 compared to HC-IOH. Although the interference fringes are quenched, the sputtered i-ZnO exhibits parasitic absorption losses of high-energy photons — a trend similar to that observed in SIT-BL — which overshadows the gain. As a result, the total optical performance of the cell is reduced to 26.4 mA/cm^2 in HC-BL4 when compared to 26.8 mA/cm^2 for HC-IOH.

External parameters of single-layer and bi-layer solar cells are reported in Table 6. For random textures, SIT-IOH outperforms SIT-BL. A drop in V_{oc} and FF is observed for the bi-layer configuration. Both solar cells exhibit top cell current-limited behaviour. SIT-IOH has 1.2% (absolute) higher η compared to SIT-BL. For periodic textures, introducing a 0.9-μm thick i-ZnO layer results in approximately the same V_{oc} and FF. An $\eta = 9.2\%$ is measured for HC-IOH and 9.7% for HC-BL4. These are also a result of a heavily current-mismatched (top-cell-limited) situation. An increase in series resistance is observed upon introducing a sputtered i-ZnO layer for both bi-layer configurations. Notably, this increase in series resistance is almost double when using 1.5-μm i-ZnO. This observation has not yet been reported in studies using LPCVD i-ZnO [19,37] or BZO [17,38]. It should be noted that the devices demonstrated in this study are not directly comparable to state-of-the-art a-Si:H/nc-Si:H configurations. Rather, the primary aim of these devices is to investigate and compare total spectral utilisation under conditions where optical interference effects are mitigated.

In summary, the optical performance of the solar cells on any texture with sputtered i-ZnO is a trade-off between the gain in photocurrent from reduced fringes and the loss of high-energy photons in the sputtered i-ZnO layer. A periodic texture combined with an i-ZnO stack with a thickness below 1 μm (sample: HC-BL4) could mitigate OC_B, OC_G, and OC_R, which is much smaller than the ≈ 2-μm thick LPCVD TCOs reported in the literature [15,19,20,23,24,39]. On the contrary, grain scattering by a 1.5-μm thick i-ZnO layer and larger crystals (sample: SIT-BL) was not as effective at removing the effects of OC_G. Since the target material influences the quality and optical absorption of the sputtered layer, the thickness that needs to be used is a compromise between parasitic absorption and light scattering. This means that a periodic hexagonal texture is the preferred combination for low-temperature sputtered i-ZnO. The reported total current density of 26.4 mA/cm^2 can yield bottom-subcell current-limited cells with 13.1 mA/cm^2 using internal reflection layer techniques and a thicker top cell.

4. Grain scattering with wide-bandgap SnO

Table 6 includes the performance of HC-SnO solar cells with a 1.0-μm-thick SnO layer implemented as a grain scatterer. When the SnO/SiO_x/IOH front electrode is used, the cell electrical performance drops significantly due to a decrease in FF caused by poor parallel resistance. We speculate that the lower parallel resistance is likely caused by shunts through the SiO_x insulation layer or the lack of a sufficient cleaning cycle between the SiO_x and IOH deposition. The SEM image and EQE of this solar cell are given in Fig. 9. The SEM images given in the inset suggest that the SnO grains exhibit a columnar crystal growth with very minimal naturally grown texture at the interface. An important observation is that a thickness of 1-μm is enough to mitigate all interference fringes caused by OC_B, OC_G, and OC_R.

The high band gap of SnO resulted in an increase in the EQE response of the top cell between 300 and 450 nm in HC-SnO compared to HC-BL4. From Table 4, a small increase of 0.4% gain in photon incoupling is observed for $R'_{300<\lambda<540}$. The same cell also shows a drop of 1.2% and 2.1% in photon flux for $R'_{550<\lambda<800}$, $R'_{800<\lambda<1200}$, respectively. These together result in an overall drop of light incoupling by 3% in HC-SnO compared to HC-BL4. The major loss is between $\lambda = 700$ nm and 1000 nm - similar to the HC-IOH in Fig. 8. The higher reflection in the 700–1200 nm range is a result of the presence of the IOH/(p)SiO:H interface in HC-SnO and HC-IOH. As seen in Fig. 2, above 700 nm IOH has the highest contrast in refractive indices with the (p)SiO:H among all TCOs used. This

Table 6
External parameters of solar cells deposited on SIT-IOH, SIT-BL, HC-IOH and HC-BL4 samples. The reported values are calculated from five cells on each textured substrate, which has the highest $V_{oc} \times FF$ value. ToC refers to top cell and BoC refers to bottom cell. Standard deviation (σ_d) of measurements is as follows: root-mean-square error of $J_{sc} = 0.7\%$ (absolute) $\sigma_d(V_{oc}) \approx 2$ mV, σ_d(FF) ≈ 0.6%, $\sigma_d(R_s) \approx 0.1$ Ω.cm^2, $\sigma_d(R_p) \approx 0.1$ kΩ.cm^2.

Sample	d_{i-ZnO} [μm]	V_{oc} [mV]	$J_{sc,ToC}$ [mA/cm^2]	$J_{sc,BoC}$ [mA/cm^2]	$J_{sc,TOT}$ [mA/cm^2]	FF [%]	R_s [$\Omega.cm^2$]	R_p [$k\Omega.cm^2$]	η [%]
SIT-IOH	0	1390	12.1	12.6	24.7	66.9	30.2	7.7	11.3
SIT-BL	1.5	1361	11.4	13.1	24.5	65.1	42.1	7.2	10.1
HC-IOH	0	1408	10.0	16.8	26.8	65.0	35.9	8.9	9.2
HC-BL4	0.9	1410	10.5	15.9	26.4	65.4	40.0	8.7	9.7
HC-SnO	1.0	1393	10.7	13.8	24.5	54.0	34.0	3.4	8.0

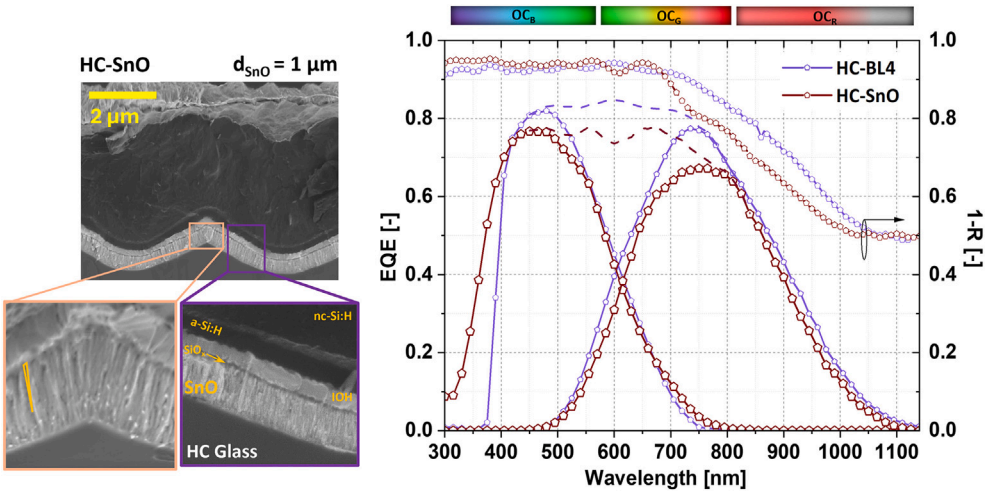

Fig. 9. EQE and 1 – *R* spectra of HC-SnO and HC-BL4 a-Si:H/nc-Si:H tandem solar cells. Dotted lines represent the total spectral utilisation of each solar cell.

means that the Fresnel reflection coefficient is higher for IOH/(p)SiO:H compared to the graded refractive indices in IOH/i-ZnO/(p)SiO:H stack. The SnO used in this demonstration exhibits heavy parasitic absorption, which reduces the total optical response of the solar cell. However, the SnO sputtering recipe can be optimised rigorously further in this case, as the TCO does not take part electrically in the cell performance. A SnO layer with high optical transmission and significantly low free carrier concentrations can be a promising route for high-performing front textures with little or no interference fringes in thin-film silicon solar cells.

5. Conclusion

This work uses a-Si:H/nc-Si:H tandem solar cells as a medium to study superstrate configuration multijunction cells with Fabry-Pérot micro-cavities. These optical micro-cavities limit the optimal light coupling in the subcells of a multijunction solar cell. Random or periodic textures demonstrate interface scattering in devices and partially mitigate the interference effect of optical cavities. However, applying textures to glass alone is insufficient to eliminate the interference effects of optical cavities completely. With interface scattering, a periodic hexagonal texture on glass breaks the coherence in light more than random textures. Furthermore, a light scattering mechanism with TCO grains is added to textures through low-temperature sputtered i-ZnO. With increasing thickness and crystal size, fringe amplitudes decrease. For a random textured glass substrate, a 1.5-µm thick i-ZnO layer could quench interference in the top cell, except for the effect of the optical cavity formed in the amorphous top cell. Whereas, hexagonal craters on glass, combined with a 0.9-µm thick i-ZnO layer, effectively mitigated fringes formed by all optical cavities in the device. It is suggested that a periodic hexagonal texture is the preferred combination for low-temperature sputtered i-ZnO. Use of a wide bandgap TCO like SnO can effectively eliminate the optical cavities, simultaneously avoiding the parasitic absorption of high-energy photons, which is otherwise absorbed by i-ZnO. The design principles discussed in this work are not restricted to a-Si:H/nc-Si:H tandem but can be extended to any thin-film multijunction solar cells consisting of layers with contrasting refractive indices.

CRediT authorship contribution statement

Govind Padmakumar: Writing – original draft, Visualization, Methodology, Formal analysis, Data curation, Conceptualization. **Federica Saitta:** Investigation. **K.P. Sreejith:** Writing – review & editing, Visualization, Formal analysis. **Paula Perez-Rodriguez:** Data curation. **René A.C.M.M. van Swaaij:** Writing – review & editing. **Arno H.M. Smets:** Writing – review & editing, Supervision, Funding acquisition, Conceptualization.

Declaration of competing interest

The authors declare the following financial interests/personal relationships which may be considered as potential competing interests:

Govind Padmakumar reports that financial support was provided by HyET Solar. If there are other authors, they declare that they have no known competing financial interests or personal relationships that could have appeared to influence the work reported in this paper.

Acknowledgements

The authors acknowledge financial and technical support from HyET Solar Netherlands B.V., Arnhem, The Netherlands. The authors thank Dr. Engin Özkol and Martijn Tijssen for their support in equipping the TCO sputtering facility used for this study.

Data availability

Data will be made available on request.

References

[1] A. Gordijn, M.N. van den Donker, F. Finger, E.A.G. Hamers, G.J. Jongerden, W.M.M. Kessels, R. Bartl, A.M.B. van Mol, J.K. Rath, B. Rech, R. Schlatmann, R.E.I. Schropp, B. Stannowski, H. Stiebig, M.C.M. van de Sanden, R.A.C.M.M. van Swaaij, M. Zeman, Flexible a-Si/µc-Si tandem modules in the helianthos project, in: 2006 IEEE 4th World Conference on Photovoltaic Energy Conference, IEEE, 2007, pp. 1716–1719, https://doi.org/10.1109/WCPEC.2006.279822

[2] A. Shah, Thin-film silicon solar cells, in: McEvoy's Handbook of Photovoltaics: Fundamentals and Applications, Elsevier Inc., 2017, pp. 235–307, https://doi.org/10.1016/B978-0-12-809921-6.00008-2

[3] T. de Vrijer, S. Miedema, T. Blackstone, D. van Nijen, C. Han, A.H.M. Smets, Application of metal, metal-oxide, and silicon-oxide based intermediate reflective layers for current matching in autonomous high-voltage multijunction photovoltaic devices, Prog. Photovolt. Res. Appl. 30 (12) (2022) 1400–1409, https://doi.org/10.1002/pip.3600

[4] H. Tan, A. Furlan, W. Li, K. Arapov, R. Santbergen, M.M. Wienk, M. Zeman, A.H.M. Smets, R.A.J. Janssen, Highly efficient hybrid polymer and amorphous silicon multijunction solar cells with effective optical management, Adv. Mater. 28 (11) (2016) 2170–2177, https://doi.org/10.1002/adma.201504483

[5] T. De Vrijer, M. Wiering, D. Van Nijen, G. Padmakumar, S. Sambamurthy, G. Limodio, A.H.M. Smets, The optical performance of random and periodic textured mono crystalline silicon surfaces for photovoltaic applications, EPJ Photovoltaics 13 (2022), https://doi.org/10.1051/epjpv/2022021

[6] A. Perot, C. Fabry, On the application of interference phenomena to the solution of various problems of spectroscopy and metrology, Astrophys. J. 9 (1899) 87, https://doi.org/10.1086/140557

[7] M. Rajibul Islam, M. Mahmood Ali, M.H. Lai, K.S. Lim, H. Ahmad, Chronology of Fabry-Perot Interferometer Fiber-Optic Sensors and Their Applications: A Review (Apr 2014), https://doi.org/10.3390/s140407451

[8] H. Tan, E. Psomadaki, O. Isabella, M. fischer, P. Babal, R. Vasudevan, M. Zeman, A.H.M. Smets, Micro-textures for efficient light trapping and improved electrical performance in thin-film nanocrystalline silicon solar cells, Appl. Phys. Lett. 103 (17) (2013) 173905, https://doi.org/10.1063/1.4826639

[9] H. Sai, T. Matsui, K. Saito, M. Kondo, I. Yoshida, Photocurrent enhancement in thin-film silicon solar cells by combination of anti-reflective sub-wavelength structures and light-trapping textures, Prog. Photovolt. Res. Appl. 23 (11) (2015) 1572–1580, https://doi.org/10.1002/pip.2594

[10] H. Sai, K. Saito, M. Kondo, Enhanced photocurrent and conversion efficiency in thin-film microcrystalline silicon solar cells using periodically textured back reflectors with hexagonal dimple arrays, Appl. Phys. Lett. 101 (17) (2012) 173901, https://doi.org/10.1063/1.4761956

[11] O. Isabella, J. Krč, M. Zeman, Modulated surface textures for enhanced light trapping in thin-film silicon solar cells, Appl. Phys. Lett. 97 (10) (2010) 101106, https://doi.org/10.1063/1.3488023

[12] G. Padmakumar, M. Criel, T. Kashyap, F. Saitta, P. Perez-Rodriguez, R.A.C.M.M. van Swaaij, A.H.M. Smets, Superimposed sacrificial texturing to enhance the optical performance in thin film solar cells, Prog. Photovolt. (2025) (in production) https://doi.org/10.1002/pip.70046

[13] H. Sai, K. Saito, M. Kondo, Investigation of textured back reflectors with periodic honeycomb patterns in thin-film silicon solar cells for improved photovoltaic performance, IEEE J. Photovolt. 3 (1) (2013) 5–10, https://doi.org/10.1109/JPHOTOV.2012.2213800

[14] J. Müller, B. Rech, J. Springer, M. Vanecek, TCO and light trapping in silicon thin film solar cells, Solar Energy 77 (6) (2004) 917–930, https://doi.org/10.1016/j.solener.2004.03.015

[15] S. Hänni, G. Bugnon, G. Parascandolo, M. Boccard, J. Escarré, M. Despeisse, F. Meillaud, C. Ballif, High-efficiency microcrystalline silicon single-junction solar cells, Prog. Photovolt. Res. Appl. 21 (5) (2013) 821–826, https://doi.org/10.1002/pip.2398

[16] J. Schroeder, J.H. Rosolowski, Light scattering in polycrystalline materials, SPIE Emerg. Opt. Mater. 297 (1981) 156–168.

[17] S. Faÿ, J. Steinhauser, N. Oliveira, E. Vallat-Sauvain, C. Ballif, Opto-electronic properties of rough LP-CVD ZnO:b for use as TCO in thin-film silicon solar cells, Thin Solid Films 515 (24 SPEC.) (2007) 8558–8561, https://doi.org/10.1016/j.tsf.2007.03.130

[18] F. Saitta, P. Kalpoe, V. Ahluwalia, G. Padmakumar, P.P. Rodriguez, G. Limodio, R. Santbergen, A.H.M. Smets, De-coupling of optical and electrical properties in front TCO using the bilayer concept for thin-film solar cells, Sol. Energy Mater. Sol. Cells 290 (2025), https://doi.org/10.1016/j.solmat.2025.113723

[19] H. Tan, E. Moulin, F.T. Si, J.-W. Schüttauf, M. Stuckelberger, O. Isabella, F.-J. Haug, C. Ballif, M. Zeman, A.H.M. Smets, Highly transparent modulated surface textured front electrodes for high-efficiency multijunction thin-film silicon solar cells, Prog. Photovolt. Res. Appl. 23 (8) (2015) 949–963, https://doi.org/10.1002/pip.2639

[20] H. Sai, K. Maejima, T. Matsui, T. Koida, M. Kondo, S. Nakao, Y. Takeuchi, H. Katayama, I. Yoshida, High-efficiency microcrystalline silicon solar cells on honeycomb textured substrates grown with high-rate VHF plasma-enhanced chemical vapor deposition, Jpn. J. Appl. Phys. 54 (8S1) (2015) 08KB05, https://doi.org/10.7567/JJAP.54.08KB05

[21] R.E.I. Schropp, C.H.M. van der Werf, M. Zeman, M.C.M. van de Sanden, C.I.M.A. Spee, E. Middelman, L.V. De Jonge-Meschaninova, P.M.G.M. Peters, A.A.M. van der Zijden, M.M. Besselink, R.J. Severens, J. Winkeler, G.J. Jongerden, Novel amorphous silicon solar cell using a manufacturing procedure with a temporary superstrate, Mater. Res. Soc. Symp. Proc. 557 (1999) 713–718, https://doi.org/10.1557/proc-557-713

[22] J.-W. Schuttauf, G. Bugnon, M. Stuckelberger, S. Hanni, M. Boccard, M. Despeisse, F.-J. Haug, F. Meillaud, C. Ballif, Thin-film silicon Triple-Junction solar cells on highly transparent front electrodes with stabilized efficiencies up to 12.8%, IEEE J. Photovolt. 4 (3) (2014) 757–762, https://doi.org/10.1109/JPHOTOV.2014.2307162

[23] J.S. Cashmore, M. Apolloni, A. Braga, O. Caglar, V. Cervetto, Y. Fenner, S. Goldbach-Aschemann, C. Goury, J.E. Hötzel, T. Iwahashi, J. Kalas, M. Kitamura, M. Klindworth, M. Kupich, G.-F. Leu, J. Lin, M.-H. Lindic, P.A. Losio, T. Mates, D. Matsunaga, B. Mereu, X.-V. Nguyen, I. Psimoulis, S. Ristau, T. Roschek, A. Salabas, E.L. Salabas, I. Sinicco, Improved conversion efficiencies of thin-film silicon tandem (MICROMORPH™) photovoltaic modules, Sol. Energy Mater. Sol. Cells 144 (2016) 84–95, https://doi.org/10.1016/j.solmat.2015.08.022

[24] J.S. Cashmore, M. Apolloni, A. Braga, O. Caglar, V. Cervetto, Y. Fenner, S. Goldbach-Aschemann, C. Goury, J.E. Hötzel, T. Iwahashi, J. Kalas, M. Kitamura, M. Klindworth, M. Kupich, G.F. Leu, J. Lin, M.H. Lindic, P.A. Losio, T. Mates, D. Matsunaga, B. Mereu, X.V. Nguyen, I. Psimoulis, S. Ristau, T. Roschek, A. Salabas, E.L. Salabas, I. Sinicco, Record 12.34% stabilized conversion efficiency in a large area thin-film silicon tandem (MICROMORPH™) module, Prog. Photovolt. Res. Appl. 23 (11) (2015) 1441–1447, https://doi.org/10.1002/pip.2642

[25] P.A. Losio, O. Caglar, J.S. Cashmore, J.E. Hötzel, S. Ristau, J. Holovsky, Z. Remes, I. Sinicco, Light management in large area thin-film silicon solar modules, Sol. Energy Mater. Sol. Cells 143 (2015) 375–385, https://doi.org/10.1016/j.solmat.2015.07.018

[26] J. Wu, Z. Wang, F. Chen, Q. Shen, L. Zhang, Chemical evolution of target surfaces during RF magnetron sputtering and its effect on the performance of TCO films, Appl. Surf. Sci. 493 (2019) 665–672, https://doi.org/10.1016/j.apsusc.2019.07.021

[27] G.T. Chavan, Y. Kim, M.Q. Khokhar, S.Q. Hussain, E.C. Cho, J. Yi, Z. Ahmad, P. Rosaiah, C.W. Jeon, A Brief Review of Transparent Conducting Oxides (TCO): the Influence of Different Deposition Techniques on the Efficiency of Solar Cells (Apr 2023), https://doi.org/10.3390/nano13071226

[28] L. Houben, M. Luysberg, P. Hapke, R. Carius, F. finger, H. Wagner, Structural properties of microcrystalline silicon in the transition from highly crystalline to amorphous growth, Philos. Mag. A: Phys. Condens. Matter Struct. Defects Mech. Prop. 77 (6) (1998) 1447–1460, https://doi.org/10.1080/01418619808214262

[29] T. de Vrijer, D. van Nijen, H. Parasramka, P.A. Procel Moya, Y. Zhao, O. Isabella, A.H.M. Smets, The fundamental operation mechanisms of nc-SiOX:h based tunnel recombination junctions revealed, Sol. Energy Mater. Sol. Cells 236 (2022), https://doi.org/10.1016/j.solmat.2021.111501

[30] P. Babal, J. Blanker, R. Vasudevan, A.H.M. Smets, M. Zeman, Microstructure analysis of n-doped nc-SiO:h reflector layers and their implementation in stable a-si:h p-i-n junctions, in: 2012 38th IEEE Photovoltaic Specialists Conference, IEEE, 2012, pp. 000321–000326, https://doi.org/10.1109/PVSC.2012.6317627

[31] G. Padmakumar, A. Balaji, M. Criel, F. Saitta, G. Limodio, P. Perez Rodriguez, R.A.C.M.M. Van Swaaij, A.H.M. Smets, Engineering of hexagonal microtextures on glass, ACS Appl. Opt. Mater. 3 (10) (2025), https://doi.org/10.1021/acsaom.5c00328

[32] G. Padmakumar, A. Balaji, F. Saitta, P. Perez-Rodriguez, R.A.C.M.M. van Swaaij, A.H.M. Smets, Hexagonal microtextured glass to achieve high optical performance in thin-film silicon solar cells, Sol. Energy 306 (2026), https://doi.org/10.1016/j.solener.2025.114292

[33] G. Padmakumar, F. Saitta, P. Sluijs, R. Boekhof, L. van der Poll, N. van Sielfhout, K.P. Sreejith, P.P. Rodriguez, L. Mazzarella, T. Savenije, T. de Vrijer, R. Vasudevan, M.E. Makkaoui, H. Lifka, E. Hamers, A.H.M. Smets, Progress in the research on the performance, processing and reliability of lightweight and flexible thin-film PV foils at TUDelft, in: 2025 IEEE 53rd Photovoltaic Specialists Conference (PVSC), IEEE, 2025, pp. 1124–1126, https://doi.org/10.1109/PVSC59419.2025.11133203

[34] S.E. Han, G. Chen, Toward the lambertian limit of light trapping in thin nanostructured silicon solar cells, Nano Lett. 10 (11) (2010) 4692–4696, https://doi.org/10.1021/nl1029804

[35] A. Chutinan, N.P. Kherani, S. Zukotynski, High-efficiency photonic crystal solar cell architecture, Opt. Express 17 (11) (2009) 8871, https://doi.org/10.1364/OE.17.008871

[36] T.A. Gessert, J. Burst, X. Li, M. Scott, T.J. Coutts, Advantages of transparent conducting oxide thin films with controlled permittivity for thin film photovoltaic solar cells, Thin Solid Films 519 (21) (2011) 7146–7148, https://doi.org/10.1016/j.tsf.2011.01.143

[37] J. Bailat, D. Dominé, R. Schlüchter, J. Steinhauser, S. Faÿ, F. Freitas, C. Bücher, L. Feitknecht, X. Niquille, T. Tscharner, A. Shah, C. Ballif, High-efficiency p-i-n microcrystalline and micromorph thin film silicon solar cells deposited on LPCVD ZnO coated glass substrates, IEEE 4th World Conf. on Photovolt. Energy Convers. 2 (2006) 1533–1536.

[38] K. Maejima, T. Koida, H. Sai, T. Matsui, K. Saito, M. Kondo, T. Takagawa, Influences of deposition temperature on characteristics of b-doped ZnO films deposited by metal–organic chemical vapor deposition, Thin Solid Films 559 (2014) 83–87, https://doi.org/10.1016/j.tsf.2013.11.137

[39] T. Matsui, K. Maejima, A. Bidiville, H. Sai, T. Koida, T. Suezaki, M. Matsumoto, K. Saito, I. Yoshida, M. Kondo, High-efficiency thin-film silicon solar cells realized by integrating stable a-si:h absorbers into improved device design, Jpn. J. Appl. Phys. 54 (8S1) (2015) 08KB10, https://doi.org/10.7567/JJAP.54.08KB10